Accepted Manuscript

Numerical and experimental characterization of the hydrodynamics and drying kinetics of a barbotine slurry spray

Daniel Sebastia-Saez, Leonor Hernandez, Harvey Arellano-Garcia, Jose Enrique Julia
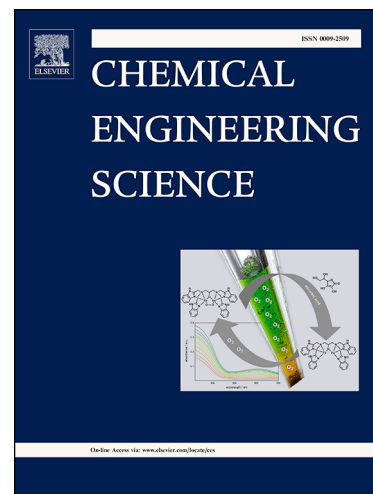
Please cite this article as: D. Sebastia-Saez, L. Hernandez, H. Arellano-Garcia, J. Enrique Julia, Numerical and experimental characterization of the hydrodynamics and drying kinetics of a barbotine slurry spray, *Chemical Engineering Science* (2018), doi: https://doi.org/10.1016/j.ces.2018.11.040

CHEMICAL ENGINEERING SCIENCE

ISSN 0009-2509

Numerical and experimental characterization of the hydrodynamics and drying kinetics of a barbotine slurry spray

Daniel Sebastia-Saez[1,*], Leonor Hernandez[2], Harvey Arellano-Garcia[1,3], Jose Enrique Julia[2,†]

[1]Department of Chemical and Process Engineering, University of Surrey, Guildford GU2 7XH, United Kingdom.
[2]Department of Mechanical Engineering, Jaume I University, Castelló de la Plana 12071, Spain.
[3]LS Prozess- und Anlagentechnik, Brandenburgische Technische Universität Cottbus-Senftenberg, D-03046 Cottbus, Germany

Spray drying is a basic unit operation in several process industries such as food, pharmaceutical, ceramic, and others. In this work, a Eulerian-Lagrangian three-phase simulation is presented to study the drying process of barbotine slurry droplets for the production of ceramic tiles. To this end, the simulated velocity field produced by a spray nozzle located at the Institute of Ceramic Technology in Castelló (Spain) is benchmarked against measurements obtained by means of laser Doppler anemometry in order to validate the numerical model. Also, the droplet size distribution generated by the nozzle is obtained at operating conditions by means of laser diffraction and the data obtained are compared qualitatively to those found in the literature. The droplet size distribution is introduced thereafter in the three-phase simulation to analyse the drying kinetics of individual droplets. The model predicts the theoretical linear evolution of the square diameter (D^2-law), and the temperature and mass exchange with the environment. The proposed model is intended to support the design and optimization of industrial spray dryers.

Keywords: spray drying; multiphase drop; CFD; laser Doppler anemometry; ceramic powder

1. Introduction. Spray drying (atomization) is a widespread process in process industry, the applications of which range from the production of powder catalysts for the chemical industry to food, micro-encapsulated products, the manufacturing of ceramic tiles, and carbon capture and storage. Most of the reported work regarding atomization has focused, however, on the food industry, whereas little attention has been given to its modelling with regard to the manufacturing of ceramic tiles [1–4]. This is despite the fact that the output control parameters of the spray drying process in the ceramic tile production chain have a significant impact on the characteristics of the final product. Gaining precise control and insight on these parameters, e.g. particle size distribution and residual humidity, is therefore crucial to quality control and proper dimensioning as well as energy analysis of the spray dryer.

*Corresponding author: Tel. +44 (0) 7719 715 575
Email: j.sebastiasaez@surrey.ac.uk

†2018.

Summary of important notation

Latin symbols		
B_M	Spalding Mass Transfer Coefficient	[-]
D_A	Binary Diffusion Coefficient (component A in air)	[$m^2 \cdot s^{-1}$]
D_{drop}	Droplet Diameter	[m]
$D_{drop,0}$	Droplet Diameter at the Beginning of the Evaporation	[m]
D_{R-R}	Rosin-Rammler Size	[m]
m_{drop}	Mass of Droplet	[kg]
$\dot{m}_{vap}$	Mass Flow Rate of Evaporating Component	[$kg \cdot s^{-1}$]
n	Rosin-Rammler Exponent	[-]
r	Radial Distance to Droplet Surface	[m]
Re_g	Reynolds Number of the Surrounding Gas Phase	[-]
t	Evaporation Time	[s]
t_{flow}	Flow Time Calculated Numerically	[s]
t_{travel}	Particle Residence Time inside the dryer	[s]
T_{drop}	Droplet Temperature	[°C]
x_{kaol}	Mass Fraction of Kaolinite	[-]
x_{water}	Mass Fraction of Water	[-]
U_∞	Velocity of the Gas Phase far from the Droplet	[$m \cdot s^{-1}$]

Greek Symbols		
β	Evaporation Rate	[$m^2 \cdot s^{-1}$]
β_{nq}	Evaporation Rate upon Non-Quiescent Surrounding Air	[$m^2 \cdot s^{-1}$]
ε_{rel}	Relative Error	[-]
λ	Wavelength	[m]
μ_g	Viscosity of Continuous Phase (air)	[$Pa \cdot s^{-1}$]
ρ_{drop}	Density of Liquid Phase (water)	[$kg \cdot m^{-3}$]
ρ_g	Density of Gas Surrounding Droplet	[$kg \cdot m^{-3}$]
ρ_{sol}	Density of Solid Particles	[$kg \cdot m^{-3}$]
ρ_{vap}	Density of Vapour Phase Evaporating from Droplet	[$kg \cdot m^{-3}$]
τ	Particle Relaxation Time	[s]

Spain is one of the major producers of ceramic tiles, along with countries such as Italy, Brazil, China, India, and Turkey. Nonetheless, ceramic tile production is the biggest economic sector in the province of Castelló (eastern Spain), with significant growth prospects in the upcoming years. To put this into perspective, the sector registered a total production of 530,000,000 m^2 in 2017 (an 8% increase with respect to 2016) with sales reaching €3,520 million in 2017 (a 7% increase with respect to 2016). Exports to other European countries, on the other hand, accounted for 47% of the sales in the same period [5]. Thus, the continuous application of new technology to improve the unit operations involved in the tile manufacturing process will substantially help in this context of competitiveness and economic relevance for the neighbouring social community.

As depicted in Figure 1, the manufacturing process begins with the quarrying, milling and mixing (1) of the raw materials in specific proportions, e.g. sand, white clays, talc, feldspar, calcite, kaolinite, and dolomite. Water is then added to the ceramic mixing (2) so as to form a slurry which is fed into the spray dryer (3). The output is a dry ceramic powder with a certain amount of residual moisture, which will be pressed (4) to the desired shape and subsequently dried and sintered (5). Finally, ornamental motifs are added to the final product (6).

Given the complex character of the multiphase flows involved in the spray drying process, the application of experimental methods at operating conditions is limited by whether they interfere or not with the flow itself. Therefore, accurate numerical models are needed in order to describe the hydrodynamics, drying kinetics and other relevant features of both the spray and the drying agent. The application of Computational Fluid Dynamics (CFD) offers a powerful and viable gateway to expand the knowledge on the multiphase transport phenomena taking place within an industrial spray dryer, and thus, to gain control over the process. Most of the previous reported studies consulted focus on the steady-state contours of diverse operating parameters within the vessel, including velocity, humidity, and concentration of solid particulate material. In this direction, Kieviet [6] obtained CFD-simulated maps of velocity and humidity within a co-current dryer as well as residence time distributions of spray droplets. Although validation of numerical models remains a hard task, Kieviet [6] also compared satisfactorily the numerical velocity and humidity profiles inside the dryer with those obtained experimentally by using hot wire anemometry and an own-designed humidity sensor. Similarly, Ali et al.

[7] developed a Eulerian-Lagrangian multiphase CFD simulation of a counter-current dryer and obtained solid phase concentration maps and residence time distributions of the discrete phase. Straatsma et al. [8] and Salem et al. [9] simulated the humidity and temperature contours of a co-current spray dryer to reduce fouling and adjust the energy consumption. Other reported studies focussing on the flow patterns of gas only and multiphase flow within the dryer including the effect of various geometric features are those of Langrish et al. [10], who studied the effect of the spray opening angles; Southwell and Langrish [11], who observed a fluctuation pattern in the flow, the spinning of which along the longitudinal axis of the vessel switches from clockwise to anti-clockwise; and Xiao et al. [12], who checked the dispersion behavior of a spray nozzle generating uniform sized particles.

The possibility of expanding CFD models by linking the drying kinetics of single droplets, namely the characteristic drying curve (CDC) and the Reaction Engineering Approach (REA), was first pointed out by Woo et al [13] in a review. Since then, a number of CFD models in the literature have included the drying kinetics of the discrete phase with a high degree of fidelity. Following that, Mezhericher et al. [14] linked a drying model previously tested with droplets in still air with a Eulerian-Lagrangian model of a co-current spray dryer. The drying kinetics was hooked to a steady-state CFD simulation using user-defined functions (UDF). The authors obtained data on the temperature, moisture content, and mass of silica slurry droplets on plots featuring droplet trajectories. The result is thus, an accurate overview of the moisture content within the dryer. However, the transient evolution of any of those variables, which would be needed to check the degree of fidelity with the theoretical temperature evolution, was omitted because of the steady-state character of their solution. Also, Tran et al. [15] linked a reduced single droplet drying (SDD) model to a CFD simulation set-up and obtained profiles of the change in water mass fraction of droplets with the vertical distance from the nozzle by using a steady-state solver. Jubaer et al. [16] compared both the perfect shrinkage and the linear shrinkage models in a transient CFD simulation to predict particle size distribution within the vessel, residence time, and particle stickiness using the concept of Discrete Particle Model (DPM) parcels. The latter authors reported the transient behavior of the water mass fraction and the stickiness criterion in the parcels, but neither the transient evolution of the droplet temperature nor their change in

diameter with time was shown and compared to the theoretically and experimentally predicted behavior.

Furthermore, a number of CFD simulations have been used to solve specific issues of the operation of spray dryers such as particle agglomeration and wall deposition. For instance, Anandharamakrishnan et al. [17] used a Eulerian-Lagrangian CFD simulation to study the residence time distribution and trajectories of spray particles in order to determine the particle sticking rate on the walls of an industrial dryer, since it may result in costly maintenance operations and hazardous situations; Woo et al. [18] studied the deposition of cotton tufts on the dryer walls; Jaskulski et al. [19] included a description of particulate material collision and agglomeration in their model and obtained maps of particle diameter and temperature within the vessel. Fletcher et al. [20], Guo et al. [21], and Roustapour et al. [22], also applied the lagrangian approach to study the hydrodynamics of the multiphase flow inside a spray dryer, although omitting the transient diameter and temperature evolution of individual droplets as well as the crust formation.

In summary, the obtaining of velocity, humidity, and temperature fields as well as particle paths within the dryer is well established in the literature. Further insight into the process is however, needed by studying the transient drying behavior of individual droplets in terms of temperature and droplet diameter change, since these two variables are intimately related to their trajectory within the dryer. Both variables are presented in this work, in order to provide more accuracy to the numerical modelling of droplet size distribution and humidity contents of the drying process output. The evolution of such individual droplets in terms of size, mass fraction of solid and liquid components is thus, obtained numerically and compared qualitatively to their theoretical behavior. The drying kinetics of individual droplets has been extensively studied experimentally in the past upon ideal conditions (static droplet with and without forced convection) by means of methods such as ultrasonic levitation and the suspended pin method [23–25]. This work aims thus, at leveraging the capabilities of CFD in order to observe the drying kinetics of multiphase droplets upon the conditions found inside an industrial spray dryer, and not only the theoretical knowledge derived from experimental methods used upon said ideal experimental conditions.

The development of the multiphase Eulerian-Lagrangian model presented in this work is summarized in Figure 2. The droplet size distribution generated by the spray

nozzle is measured by laser diffraction analysis following the methodology described in section 3.1 and subsequently introduced in the three-phase simulation of the spray jet, the numerical methodology of which is described in section 3.3. Validation of the selected physical models of the numerical set-up is attained by comparison of the velocity fields obtained numerically with those obtained experimentally by using laser Doppler anemometry (LDA). The output from the model is simulated data on the drying process of the characteristic droplet size (Rosin-Rammler size), which are presented and discussed in section 5.

The interplay between trajectory and individual droplet drying behavior presented in this work can be used in the future as a powerful tool to select the dimensions of the spray dryer and the temperature and humidity conditions of the drying agent, adding to the general effort towards minimising energy consumption, particularly in the case of ceramic tile manufacturing.

2. Theoretical background

The evaporation of droplets follows the D^2-law, which was first developed assuming quiescent air in the surroundings of the droplet, but has proved to hold also when there is a certain relative velocity between the drop and the drying agent [23].

Several assumptions are considered for the derivation of the D^2-law. Firstly, the evaporation occurs at quasi-steady regime, that is to say, the velocity of the vapour leaving the drop is significantly greater than the velocity at which the liquid-gas interface, i.e. the surface of the droplet, changes during the evaporative process. Secondly, the concentration of the species in the boundary layer formed in the vicinity of the gas-liquid interface matches the saturation conditions. Finally, the temperature of the droplet, the densities of both the gas and the liquid phase, and the diffusion coefficient are assumed to remain constant during the process.

Upon these conditions, one can express the mass flux of evaporating component in the radial dimension by the following Eqn. (1), which establishes that the flow rate of vapour of a certain component A in the liquid droplet leaving the surface of the droplet at a radial distance r from the droplet surface $\dot{m}_{vap}(r)$ is the result of adding two terms, the first one of which accounts for the mass transfer caused by advection, and the second describes the Brownian diffusion caused by the concentration gradient of the particular species being considered

$$\dot{m}_{vap}(r) = \dot{m}_{vap}(r)x_A - \rho_{vap}D_A\frac{dx_A}{dr}, \tag{1}$$

where x_A denotes the mass fraction of the component A at the droplet surface, ρ_{vap} represents the density of the vapour phase, and D_A is the binary diffusion coefficient of the component A in air.

Elaborating on Eqn. (1), one arrives to the following first order ordinary differential equation (Eqn. 2)

$$\frac{dx_A}{dr} = -\frac{\dot{m}_{vap}(1-x_A)}{\pi D_{drop}^2 \rho_{vap}D_A}, \tag{2}$$

the solution of which considering the boundary condition $x_A(r \to \infty) = x_{A,\infty}$ is

$$x_{A,\infty} = 1 - \frac{1 - x_{A,int}}{e^{\left(-\frac{\dot{m}_{vap}}{2\pi\rho_{vap}D_A D_{drop}}\right)}}, \tag{3}$$

where $x_{A,s}$ is the mass fraction of the component A at the gas-liquid interface, i.e. the surface of the droplet, and D_{drop} is the diameter of the droplet.

The mass flow rate of vapour into the surroundings $\dot{m}_{vap}$ can now be isolated from Eqn. (3) as

$$\dot{m}_{vap} = 2\pi D_{drop}\rho_{vap}D_A ln[1 - B_M], \tag{4}$$

where the Spalding mass transfer coefficient B_M is defined as

$$B_M = \frac{x_{A,\infty} - x_{A,int}}{x_{A,int} - 1}. \tag{5}$$

One can now equate the flow rate of evaporated mass $\dot{m}_{vap}$ to the rate of change of the mass of the droplet m_{drop} as

$$\frac{dm_{drop}}{dt} = -\dot{m}_{vap}; \ m_{drop} = \rho_{drop}\pi\frac{D_{drop}^3}{6}, \tag{6}$$

where ρ_{drop} is the density of the droplet, and t is the evaporation time.

The following differential equation (Eqn. 7) is obtained by combining Eqns. (4) and (6). Eqn. 7 relates the change in diameter of the droplet during the evaporation time with the properties of the fluids involved and the conditions far away from the gas-liquid interface:

$$\frac{dD_{drop}^2}{dt} = -8\frac{\rho_{vap}}{\rho_{drop}}D_A ln[1 - B_M]. \tag{7}$$

Its solution gives us the D²-law as

$$D_{drop}^2(t) = D_{drop,0}^2 - \beta t, \tag{8}$$

Where the subscript 0 denotes the droplet diameter when the evaporation starts and β is the evaporation rate.

The D^2-law predicts, thus, a linear evolution of the square diameter of the droplet with time, i.e. the Constant Rate Period or CRP, which takes place at constant temperature (wet bulb temperature). Once a crust is formed on the droplet surface due to the presence of the solid phase, the diameter remains constant and a significant increase in temperature occurs due to sensible heat transfer from the surrounding gas to the droplet, i.e. the Falling Rate Period or FRP. This behavior has been reproduced in the present simulations. The D^2-law will therefore be used to compare qualitatively the numerical data obtained in this work with the theory.

In the case of droplets within air in non-quiescent conditions, which is the case inside the pilot-scale spray dryer, the evaporation rate β must be corrected by using the Frössling correlation, which reads

$$\frac{\beta}{\beta_{nq}} = 1 + 0.3Re_g^{0.27}, \tag{9}$$

to obtain the evaporation rate upon non-quiescent conditions β_{nq}, being the Reynolds number of the gas phase defined as

$$Re_g = \frac{\rho_g U_\infty D_{drop}}{\mu_g}, \tag{10}$$

where U_∞ represents the velocity of the surrounding air far away from the surface of the droplet, and ρ_g and μ_g are the density and the dynamic viscosity of the gas phase, respectively.

3. Methods. Two experimental set-ups have been used in this work in order to: 1) complement the simulation by determining the droplet size distribution generated by the nozzle of the pilot-scale spray dryer, which was introduced in the CFD set-up, and 2) validate the velocity field obtained numerically by comparison against the experimental measurements obtained by means of Laser Doppler anemometry (LDA). The numerical approach is described in subsection 3.3.

3.1. Droplet size distribution (Laser Diffraction Analysis)

Measurements of the droplet size distribution generated by the spray nozzle were undertaken using a laser diffraction device (Malvern Spraytec 2600). Two values of the water flow rate (0.41 L/min and 0.83 L/min), two gauge pressure values for the air flow (1.5 bar and 2.0 bar), and three values for the vertical distance from the

nozzle (2.0, 7.5, and 16.0 mm) were considered in order to qualitatively compare the results obtained with available data in the literature. Table 1 summarises the experiments performed and their parameters. The measurements were taken in the symmetry axis of the jet by means of a 5 mW He-Ne laser beam with a wavelength λ=632.8 nm. Each experiment was run during 20 s, which ensured a sufficient data to calculate the Sauter Mean Diameter ($\overline{SMD}$).

3.2. Laser Doppler Anemometry. A schematic illustration of the LDA experimental set-up is represented in Figure 3. The initial Ar^{+} laser beam (0.5 W) is split by a Bragg cell (Fiberflow[TM]), and subsequently converged at a target spot using a lens with a focal distance of 40 cm. The velocity field is determined by measuring the successive peaks in the signal caused by the impact of the laser beams on tracer particles. Incense smoke was used as a tracer in this experiment owing to its particles being light and small enough so as to be carried by the continuous phase (Stokes No. $St = \rho_{sol}D_{drop}^2/18\mu_g\,\tau \approx 0.0006$ [26]), but detectable by the laser [28]. The doping of the pressurized air with the incense smoke tracer was achieved by inserting a convergent-divergent nozzle in the line between the nozzle and the reservoir, where incense sticks were burnt. A green laser beam (λ=514.5 mm) and a red beam (λ=488 mm), both with a frequency f=500 kHz, were used to determine the vertical and the horizontal components of the velocity field, respectively. Data recorded to each measurement point were sampled during 30 s, which allowed to collect up to 20,000 values. The signal processor FVA 58N40 and the software Floware[TM] were used to analyse the data. The measurement points were selected in a sufficient number so as to reconstruct the structure of the jet.

Pressurized air from the lines available in the laboratory at 0.5 bar gauge pressure was fed into the nozzle. Before the LDA experiments, water at a flow rate of 0.41 l/min was also circulated from a reservoir in the same laboratory and injected into the spray nozzle in order to obtain CCD images of the jet, with the objective of determining the measurement points of interest (one of these images has been included in Figure 3). The nozzle, along with its auxiliary equipment were placed outside the lab-scale dryer to avoid the effect of its opaque walls. The inset CCD photograph of the jet shows a distinction between a denser area of droplets and its surroundings. The measurement spots were all selected inside the dense part of the jet (up to 20,000 measurements in each measurement spot).

3.3. Numerical methodology. Parallel runs of the three-phase simulation set-up using ANSYS CFX v19.1 in a machine with 4 CPUs were performed. A 2D structured computational grid comprised of 35,600 nodes (200 nodes in the vertical direction and 178 in the horizontal direction, with the minimum distance between nodes being 500 μm) was developed by means of the blocking strategy in ANSYS ICEM to obtain the results shown in this work. A schematic illustration of the lab-scale spray dryer available at the Ceramic Technology Institute of Castelló (Spain) is depicted in Figure 4, along with the detail of the computational domain and its relation with the geometry of the lab-scale spray dryer. A coarser (100 × 58 nodes), and a finer mesh (400 × 358 nodes) were developed, in order to check the effect of the grid spacing on the results (Figure 5). The mesh resolution does not change the development of the jet structure; neither does it change the flow time at which the jet gets to the upper part of the domain. There is a difference however, in the formation of some eddies within the numerical domain. The fine mesh has a minimum grid spacing of 250 microns, which highlights the fact that high-fidelity simulations of such a turbulent multiphase flow inside the dryer is beyond current computational capacities. The three meshes feature local refinement on the axis of the jet and the area next to the spray injection cone. The Eulerian phase, i.e. the air of the spray, is defined as a mixture of dry air and water vapour, with an inlet temperature of 900°C and zero initial water vapour content. The temperature and humidity conditions of the continuous phase were selected in order to clearly visualize the drying process of the droplets. Following sufficiently long particle trajectories within the domain, these parameters allowed us to check whether the CFD model could reproduce the behavior predicted by the D^2-law. The velocity profile obtained by means of the LDA

technique at a vertical distance of 2.5 mm from the nozzle was introduced as the boundary condition for the spray inlet (see Figure 4 to check placement of the boundary conditions). A customized discrete phase is defined (barbotine), which is an ideal mixture of liquid water and kaolinite $Al_2Si_2O_5(OH)_4$ (density of 2650 kg·m^{-3} and a specific heat capacity of 750 J·kg^{-1}·K^{-1}) in the proportions of 0.4/0.6 mass fraction, respectively. The discrete phase was injected at a mass flow rate of 0.0014 kg·s^{-1}, injection velocity of 14 m·s^{-1}, and ambient temperature (25°C). Non-slip wall boundaries are set on either side of the numerical domain and on the top boundary. Openings are set as boundary conditions on the rest of the domain boundaries. Only the spray (formed by air and solid-liquid droplets) is considered in the simulation and not the drying air, the entrance of which is depicted in the schematic of the dryer (Figure 4). The discrete phase is injected according to the average value of the velocity profile at a vertical distance of 2.5 mm and according to a cone with an opening angle of 34° measured on photographs taken with a CCD camera. As for the evaporation of water from the droplets into the dry air, an additional material was created, in which the saturation properties of water are defined according to Antoine's equation. The calculations are carried out in a transient regime with a time step of 0.01 s until 4.5 s flow time t_{flow}. The maximum number of iterations per time step allowed in order to achieve convergence was 10; and the residual target value is 10^{-3}. The results of a previous steady state single phase calculation (featuring only the continuous phase) at a flow time t_{flow}=1.5 s were used as initial conditions (Figure 5). The turbulence model selected is the k-ε. Other complex phenomena such as particle collision, coalescence and secondary breakup are omitted. The option fully coupled is selected to describe the momentum exchange between the continuous and the discrete phase. The Ranz-Marshall model was the option selected to describe heat transfer. The simulation set-up described here gave way to values of the residuals (RMS) below 10^{-3} in the three meshes used (Figure 6). The medium mesh was used thereafter as a trade-off between accuracy and computational time.

4. Results and discussion

4.1. Droplet size distribution.

Each laser diffraction experiment described in Table 1 was performed three times to determine the droplet size distribution generated by the nozzle. The results of the repeatability analysis are presented in Table 2.

The relative error ε_{rel} in Table 2 is defined as the range between the maximum and the minimum value divided by the average of the three repetitions (denoted as $\overline{SMD}$). Good repeatability is achieved, with the maximum relative error being 2.28% for experiment #5. The results of the repeatability analysis allow to conclude that the experimental methodology applied for the determination of the droplet size distribution was consistent and reliable.

To facilitate the comparison between the data obtained, the results of the laser diffraction analysis were plotted against the vertical distance from the nozzle (height from nozzle) in subplot a included in Table 2, which also includes the effect of the pressure; and against the liquid flow rate in subplot b (also in Table 2). In both subplots a shaded area has been included with the same colour as the markers in order to gather data points obtained upon similar parameters. Two series of data, corresponding to the pressure levels considered in the experiments, are plotted in Table 2, which allow to conclude that greater air pressure causes greater break-up, and thus resulting in smaller droplets. A turning point appears in the trend defining the relation between the SMD and the height from the nozzle. Droplet break-up, coalescence and differences in linear momentum of the droplets according to their size are hypothesized as the possible causes of this behavior, which has not been investigated in this work and will be considered in the future. With regards to the effect of the liquid flow rate, four pairs of experiments were compared, keeping the air pressure and the vertical distance from the nozzle at a constant value in each pair. In all four pairs of experiments, an increase of the Sauter Mean Diameter of the distribution was found with the liquid flow rate. Juslin et al. [27] studied the effect of several variables, including the liquid flow rate and the air pressure, on the droplet size distribution generated by a spray nozzle in a factorial (3^3) experiment. The results in this work show qualitative consistency with the data reported by the latter authors for both the liquid flow rate and the air pressure. After successful qualitative comparison with reported data, the distribution corresponding to 0.41 l/min, 0.5 bar gauge pressure, and a vertical distance from the nozzle of 2 mm (experiment #1) was implemented in the CFD model. The probability histogram and its corresponding

cumulative curve is depicted in Figure 7, which also shows the parameters of the curve fitting to a Rosin-Rammler distribution, with an R^2 coefficient equal to 0.997.

4.2. Validation of the CFD hydrodynamics. Values of both the axial and radial velocity were obtained at different locations by using the experimental methodology and the numerical set-up described in sections 3.2 and 3.3, respectively. Figure 8 shows the validation of the velocity field by comparison between the data obtained by both methods, showing fair agreement between them. One side of the jet has been shown in the Figure due to its symmetry. Smaller velocity values than in the rest of the experimental data series, must be noted in the vicinity of the symmetry axis of the spray at a vertical distance of 100 and 150 mm from the nozzle. These smaller values are tagged as swirl on the plot. The swirl is caused by the geometry of the nozzle, the inner part of which consists of a homogenization cavity where the air is injected tangentially.

Both methods detect a certain degree of air entrainment in the area next to the boundary of the nozzle (also tagged on Figure 8). The entrainment velocities are of the same magnitude as those of the jet itself. To enhance the visualization of this phenomenon, a grey vertical line has been included in the plot of axial velocity at a vertical distance of 2.5 mm from the nozzle. This line allows the reader to visualise the limit of the nozzle opening, which has a circular shape with a diameter 2.8 mm. The valley between the two consecutive parabolic sections observed in the plot of axial velocity at 2.5 mm vertical height matches the position of the nozzle opening outer boundary (the grey vertical line). Negative values are observed in the plot of radial velocity at a vertical distance 2.5 mm for the range of x values which correspond to the nozzle opening. These are attributed to the geometry of the nozzle, which has been depicted in Figure 3 and has a conical shape, meaning that the horizontal component of the velocity vector is directed towards the symmetry axis of the jet.

In summary, the results obtained numerically represent the trend and values of those obtained experimentally with a high degree of accuracy, providing a basis to justify the selection of the models that conform the CFD set-up.

4.3. CFD results of the droplet drying process. The transient drying process of a characteristic droplet with the size of the Rosin-Rammler diameter D_{R-R}=321 µm is represented in Figure 9, where the two stages of the drying process, i.e. constant rate period (CRP) and falling rate period (FRP) can be observed. Three

different particle trajectories have been tracked during a flow time t_{flow} of approximately 4.5 s. The different trajectories have been selected in order to check different particle travel times. The values of the latter for trajectories 1, 2, and 3 are approximately t_{travel}=1.7, 1.1, and 0.9 s, respectively. A well-defined linear decrease in square diameter is observed for all of the trajectories up to the formation of the crust, after which the square diameter of the droplet D_{drop}^2 remains constant at 52,284 μm². The latter matches the diameter that corresponds to the initial mass fraction and density of the solid component (kaolinite). Both stages of the drying process, i.e. CRP and FRP, are thus, well reproduced by the model. The results also show that the particle following trajectory #3 does not spend enough time in the domain to dry out, and thus, it does not reach the FRP stage. Therefore, where particles corresponding to trajectories #1, and #2 reach a plateau in both square diameter and mass fraction of the liquid and solid component, only the linear decrease corresponding to CRP is observed for the droplet following trajectory #3 before it abandons the numerical domain. Snapshots of the trajectories are included in Figure 9, which allow the user to determine the exact instant and location where the crust formation occurs. Upon extension to 3D geometries in order to represent the entirety of the dryer, the capability of this model to determine when and where the particles should dry out will be key to determine the adequate dimensions of the drying vessel and the parameters of the drying agent.

The theoretical evolution of the droplet temperature during the drying process is also represented in the plot. A sharp increase in temperature must occur according to theory when a stable crust forms after evaporation at a constant temperature. The sharp temperature increase is caused by the depletion of the liquid phase, which results in sensible heat (and not latent heat) being transferred to the droplet. The results show that the CRP occurs at constant temperature (T_{drop}=25°C), before giving way to a sharp increase at the beginning of the FRP, i.e. when the crust forms. The temperature during the FRP shows fluctuations with a smaller order of magnitude than the qualitative increase observed between the CRP and the FRP. Where the temperature change between both drying stages ΔT_{drop} lies in the hundreds, the fluctuations taking place after the formation of the solid crust oscillate around 90°C.

The results also show the evolution of the mass fraction of both components present in the discrete phase, i.e. droplets comprised of solid kaolinite and liquid water. The plot shows the depletion of the liquid component (x_{water}=0), with the solid mass fraction attaining the value of x_{kaol}=1. Depletion of the liquid phase (x_{water}=0) occurs at a particle travel time which matches that of the formation of the solid crust (transition between CRP and FRP) in the plot corresponding to the time evolution of the square diameter, and the sharp increase observed in the time evolution of the temperature of the droplet.

5. Conclusions

A look at the work published so far reveals the existence of maps of velocity, humidity, and pressure within the industrial spray dryer obtained by means of Computational Fluid Dynamics (CFD). The drying kinetics of individual droplets (and their subsequent change in diameter related to their trajectory) is still missing. Although a grid sensitivity study reveals that a complete description of the turbulent multiphase flow within the dryer is far beyond current computational capacities, the purpose of this model is therefore, to take a step forward towards the transient study of the heat and mass transfer of individual solid-liquid multiphase droplets by developing a CFD model which reproduces the D^2-law in order to compare trajectories and determine the exact instant and location where the solid crust forms. Moreover, to date, the drying kinetics of individual droplets has been studied experimentally by using the suspended pin method and the ultrasonic levitation method, both of which neglect the effect of the chaotic flow that occurs inside an industrial spray dryer. The numerical model presented here gives thus, the opportunity to check the drying behavior of individual droplets upon the complex conditions found within an industrial spray dryer.

The model follows a Eulerian-Lagrangian approach, which allows the user to track the trajectories of a particulate phase, i.e. the discrete phase, within a continuous fluid domain. The particle size distribution of multiphase droplets generated by the nozzle of the pilot-scale spray dryer available at the Ceramic Technology Institute of Castelló (Spain) was obtained experimentally by means of laser diffraction analysis and subsequently fitted to a Rosin-Rammler distribution. The experimental results of the droplet size distribution as a function of the liquid flow rate, air pressure and height from the nozzle were compared qualitatively to results found in the literature to check their validity, with positive results. The repeatability of the results is checked

by performing each experiment three times, reaching the conclusion that the methodology used to determine the droplet size distribution was adequate. The characteristic Rosin-Rammler size was used as the initial diameter of the droplets injected into the CFD model.

Validation of the hydrodynamics of the CFD model is accomplished by comparison between the numerical results of the air velocity field generated by the spay nozzle to those obtained by means of Laser Doppler Anemometry at different vertical distances. The selection of the physical models in the simulation is thus, justified given the satisfactory comparison to the experimental measurements.

The model represents satisfactorily the theoretical drying behavior of individual droplets. A clear stage where the evolution of the droplet square diameter decreases linearly with time, i.e. the constant rate period or CRP, is observed, followed by a second stage where the square diameter remains constant at a value that corresponds to a kaolinite mass fraction x_{kaol}=1, i.e. the falling rate period or FRP. Both drying stages are predicted by the classical D^2-law and reproduced with the numerical model presented herein. The evolution of the temperature is also studied. A first stage is found which unfolds at constant temperature until the end of the CRP. The first stage is followed by a sharp rise when the solid crust forms, after which fluctuations in the droplet temperature are observed caused by the droplet travelling through areas at different temperatures. The model predicts thus, the loss of the liquid fraction at a constant temperature (latent heat) and the sharp increase caused by the depletion of the liquid phase (sensible heat).

The present transient CFD model is thus, capable of determining the instant and location of solid-liquid multiphase droplets crust formation. The model proves itself as a powerful tool to support the design of an industrial spray dryer, given its capability to study the hydrodynamics and drying kinetics of individual droplets across a range of initial diameters.

Acknowledgements

REFERENCES

[1] C. Eckert, V.G. Serpa, A.C.F. dos Santos, S.M. da Costa, V. Dalpubel, D.N. Lehn, and C.F.V. de Souza. Microencapsulation of Lactobacillus plantarum ATCC 8014 through spray drying and using dairy whey as wall materials. LWT - Food Science and Technology 82:176–183, 2017.

[2] R. Kuriakose and C. Anandharamakrishnan. Computational fluid dynamics (CFD) applications in spray drying of food products. Trends in Food Science and Technology 21:383–398, 2010.

[3] L. Kavoshi, A. Rahimi, and M. Hatamipour. CFD modeling and experimental study of carbon dioxide removal in a lab-scale spray dryer. Chemical Engineering Research and Design 98:157–167, 2015.

[4] I. Schmitz-Schug, U. Kulozik, and P. Foerst. Modeling spray drying of dairy products – impact of drying kinetics, reaction kinetics and spray drying conditions on lysine loss. Chemical Engineering Science 141:315–329, 2016.

[5] ASCER (Asociación Española de Fabricantes de Azulejos y Pavimentos Cerámicos). Las cifras del sector en 2017, (2018).

[6] F. Kieviet, Modelling quality in spray drying, Ph.D. thesis, Eindhoven University of Technology, Eindhoven. The Netherlands, 1997.

[7] M. Ali, T. Mahmud, P.J. Heggs, M. Ghadiri, A. Bayly, H. Ahmadian, and L.M. de Juan. CFD simulation of a counter-current spray drying tower with stochastic treatment of particle-wall collision. Procedia Engineering 102:1284–1294, 2015.

[8] J. Straatsma, G.V. Houwelingen, A. Steenbergen, and P.D. Jong. Spray drying of food products: 1. simulation model. Journal of Food Engineering 42:67–72, 1999.

[9] A. Salem, M. Ahmadlouiedarab, K. Ghasemzadeh. CFD approach for the moisture prediction in spray chamber for drying of salt solution. Journal of Industrial and Engineering Chemistry 17:527–532, 2011.

[10] T.A.G Langrish, J. Williams, and D.F. Fletcher. Simulation of the effects of inlet swirl on gas flow patterns in a pilot-scale spray dryer. Chemical Engineering Research and Design 82(7):821–833, 2004.

[11] D.B Southwell and T.A.G. Langrish. The effect of swirl on flow stability in spray dryers. Chemical Engineering Research and Design 79(3):222–234, 2001.

[12] J. Xiao, Y. Li, O.A. George, Z. Li, S. Yang, M.W. Woo, W.D. Wu, and X.D. Chen. Numerical investigation of droplet pre-dispersion in a monodisperse droplet spray dryer. Particuology 38:44–60, 2018.

[13] M.W. Woo, W.R.W. Daud, A.S. Mujumdar, M.Z.M. Talib W.Z. Hua, and S.M. Tasirin. Comparative study of droplet drying models for CFD modelling. Chemical Engineering Research and Design 86:1038–1048, 2008.

[14] M. Mezhericher, A. Levy, and I. Borde. Spray drying modelling based on advanced droplet drying kinetics. Chemical Engineering and Processing: Process Intensification 49:1205–1213, 2010.

[15] T.T.H. Tran, M. Jaskulski, and E. Tsotsas. Reduction of a model for single droplet drying and application to CFD of skim milk spray drying. Drying Technology 35(13):1571–1583, 2017.

[16] H. Jubaer, S. Afshar, J. Xiao, X.D. Chen, C. Selomulya, and M.W. Woo. On the importance of droplet shrinkage in CFD-modeling of spray drying. Drying Technology.

[17] C. Anandharamakrishnan, J. Gimbun, A. Stapley, and C. Rielly. A study of particle histories during spray drying using computational fluid dynamic simulations, 2002. In 16th International Drying Symposium. Hyderabad, India 9–12 November (IDS 2008).

[18] M. Woo, L. Che, W. Daud, A. Mujumdar, and X. Chen. Highly swirling transient flows in spray dryers and consequent effect on modelling of particle deposition. Chemical Engineering Research and Design 90:336–345, 2012.

[19] M. Jaskulski, P. Wawrzyniak, and I. Zbiciński, CFD simulations of droplet and particle agglomeration in an industrial counter-current spray dryer, Advanced Powder Technology 29:1724–1733, 2018.

[20] D. Fletcher, B. Guo, D. Harvie, T. Langrish, J. Nijdam, and J. Williams. What is important in the simulation of spray dryer performance and how do current CFD models perform. Applied Mathematical Modelling 30:1281–1292, 2016.

[21] B. Guo, T.A.G. Langrish, D. Fletcher. Simulation of the agglomeration in a spray using Lagrangian particle tracking. Applied Mathematical Modelling 28:273–290, 2004.

[22] O.R. Roustapour, M. Hosseinalipour, B. Ghobadian, F. Mohaghegh, and N.M. Azad, A proposed numerical-experimental method for drying kinetics in a spray dryer, Journal of Food Engineering 90:20–26, 2009.

[23] B.A. Zaitone. Drying of multiphase single droplets in ultrasonic levitator. Ph.D. thesis. Technische Universität Darmstadt, Darmstadt. Germany, 2009.

[24] W. Ranz and J. Marshall, Evaporation from drops 1, Chemical Engineering Progress 48141–144, 1952.

[25] W. Ranz and J. Marshall. Evaporation from drops 2. Chemical Engineering Progress 48:173–180, 1952.

[26] Y. Chang, H. Lee, H. Tseng, The formation of incense smoke, Journal of Aerosol Science 39:39–51, 2007.

[27] L. Juslin, O. Antikainen, P. Merkku, J. Yliruusi, Droplet size measurement: II. effect of three independent variables on parameters describing the droplet size distribution from a pneumatic nozzle studied by multilinear stepwise regression analysis, International Journal of Pharmaceutics 123:257–264, 1995.

LIST OF FIGURES

Ceramic tile manufacturing process
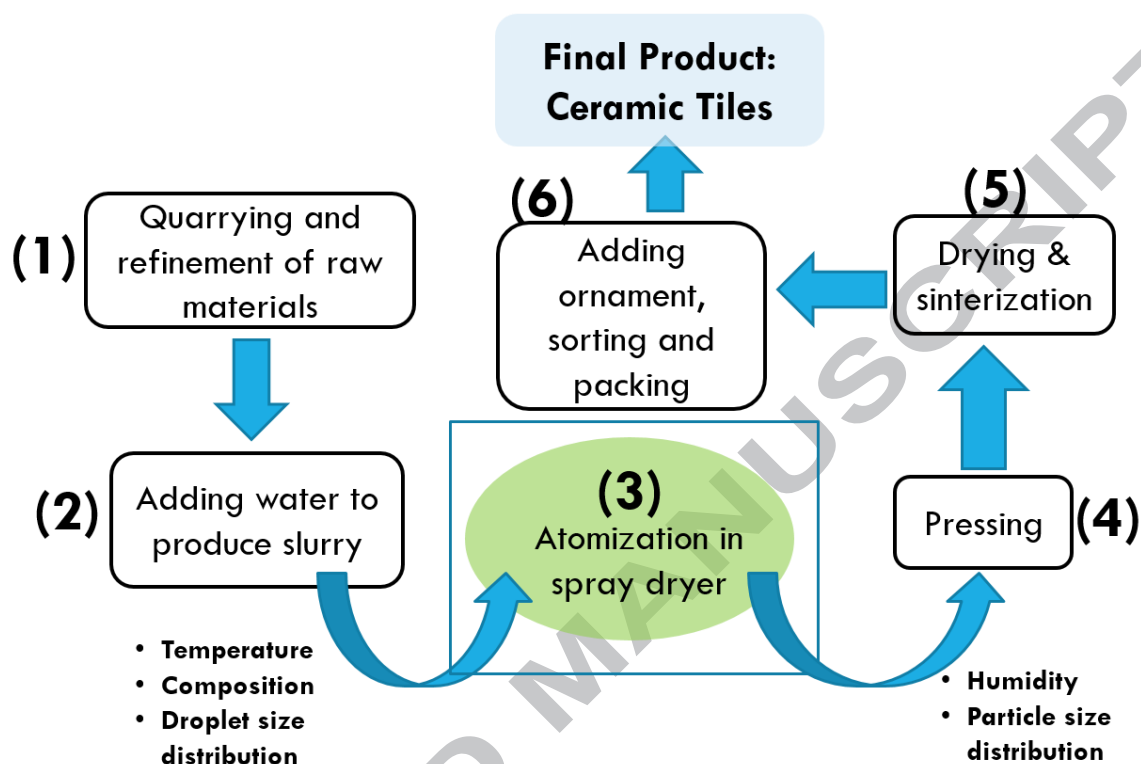
Figure 1 Schematic illustration of the ceramic tile production chain. The graph sets the context of the development of the present CFD model. Spray drying constitutes the central part of the process and has been highlighted in the schematic using a green background. The input (temperature, composition, and droplet size distribution) and output parameters (humidity and particle size distribution) to the spray drying process determine the quality of the final product and are included in the bullet points.
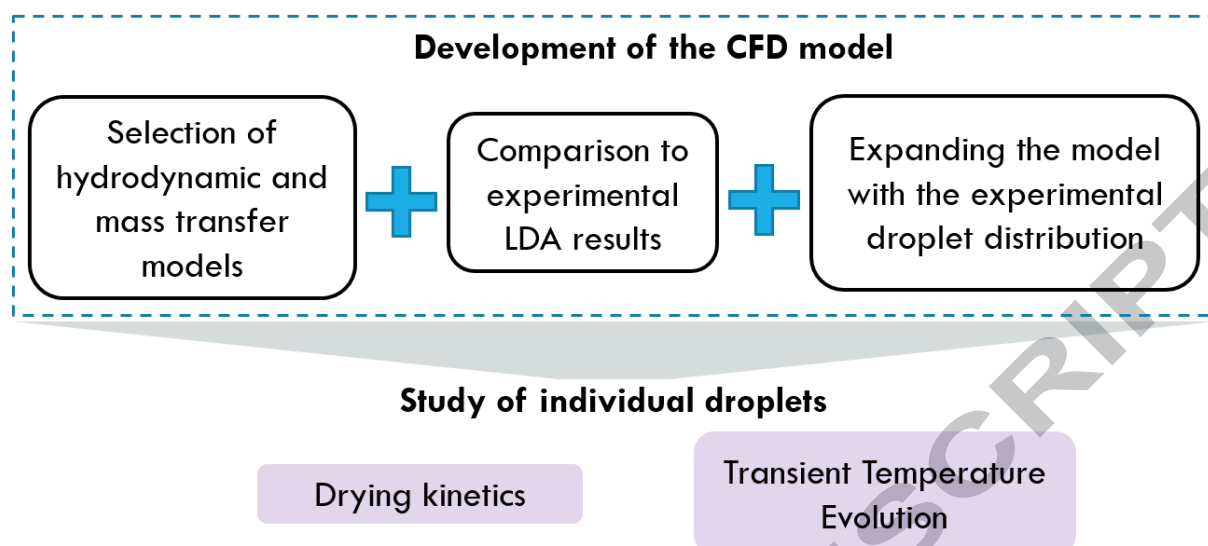
Figure 2 This schematic illustration summarizes the strategy followed to develop the present CFD model (the three boxes within the dashed line) and the general objective of the study. The selection of the hydrodynamic, heat transfer, and evaporation models is followed by the introduction of the droplet size distribution generated by the spray nozzle. The latter is obtained using laser diffraction analysis. The validation of the hydrodynamics of the CFD simulation is accomplished by comparison with the velocity field obtained using laser Doppler anemometry. The target variables that the CFD simulation produces are shown at the bottom of the Figure (marked in purple).
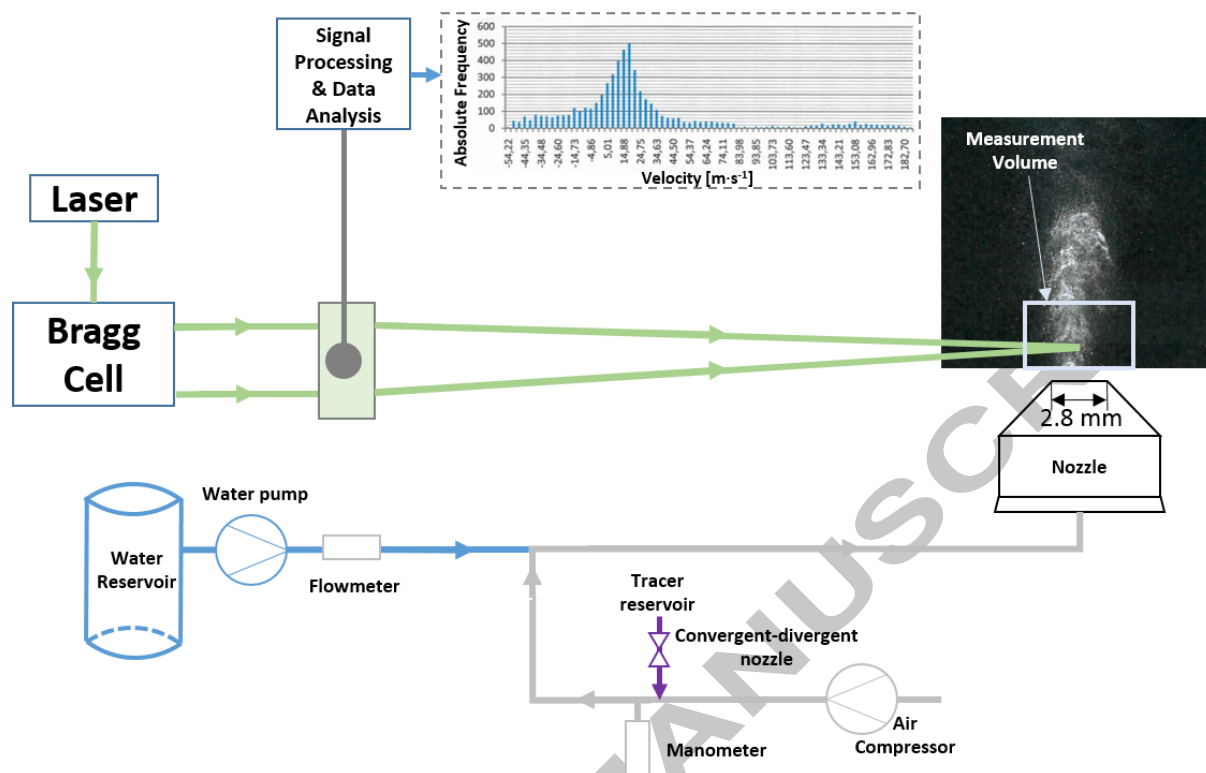
Figure 3 Schematic illustration of the Laser Doppler Anemometry (LDA) experimental set-up.
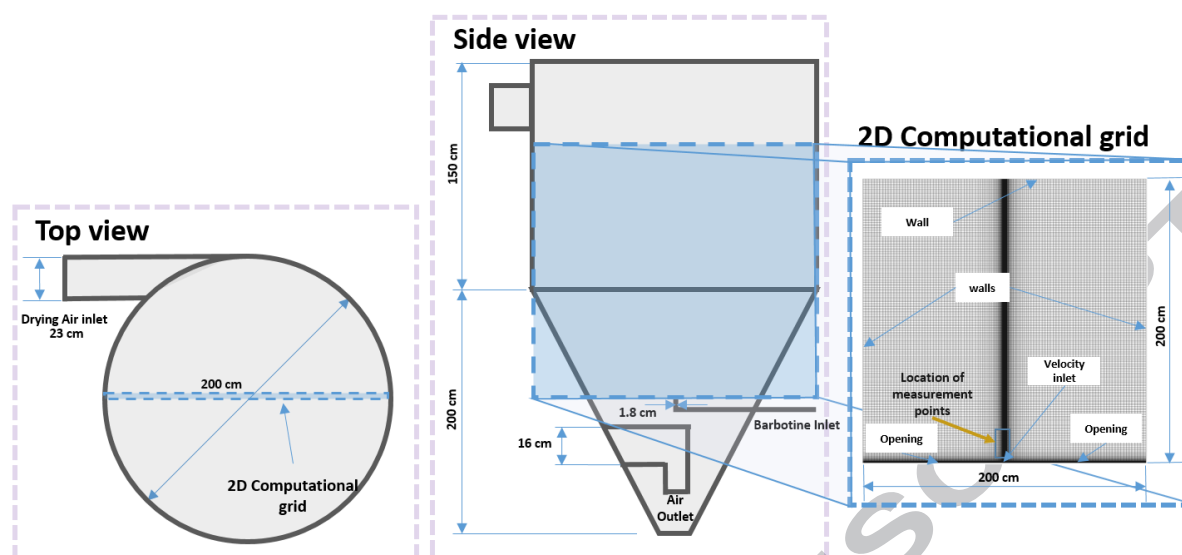
Figure 4 Schematic illustration of the pilot-scale spray dryer available at the Ceramic Technology Institute of Castelló (Spain) and its relation with the 2D computational grid used in the CFD model.
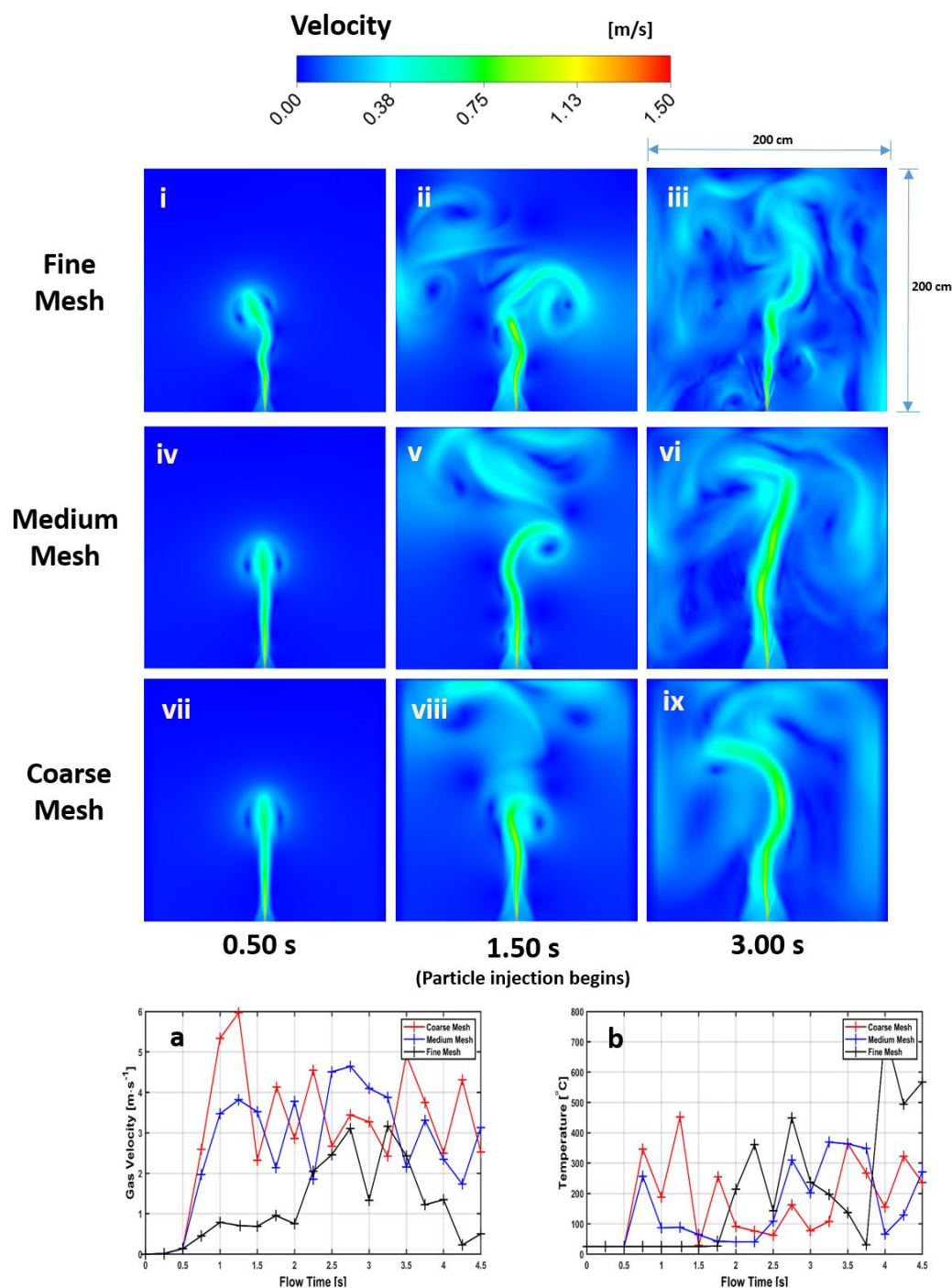
Figure 5 Time evolution of the velocity field for the three meshes tested (subplots i-ix). Effect of the grid size on the gas velocity (a), and temperature (b) of a monitor point located in the jet axis at 1.5 m from the nozzle.
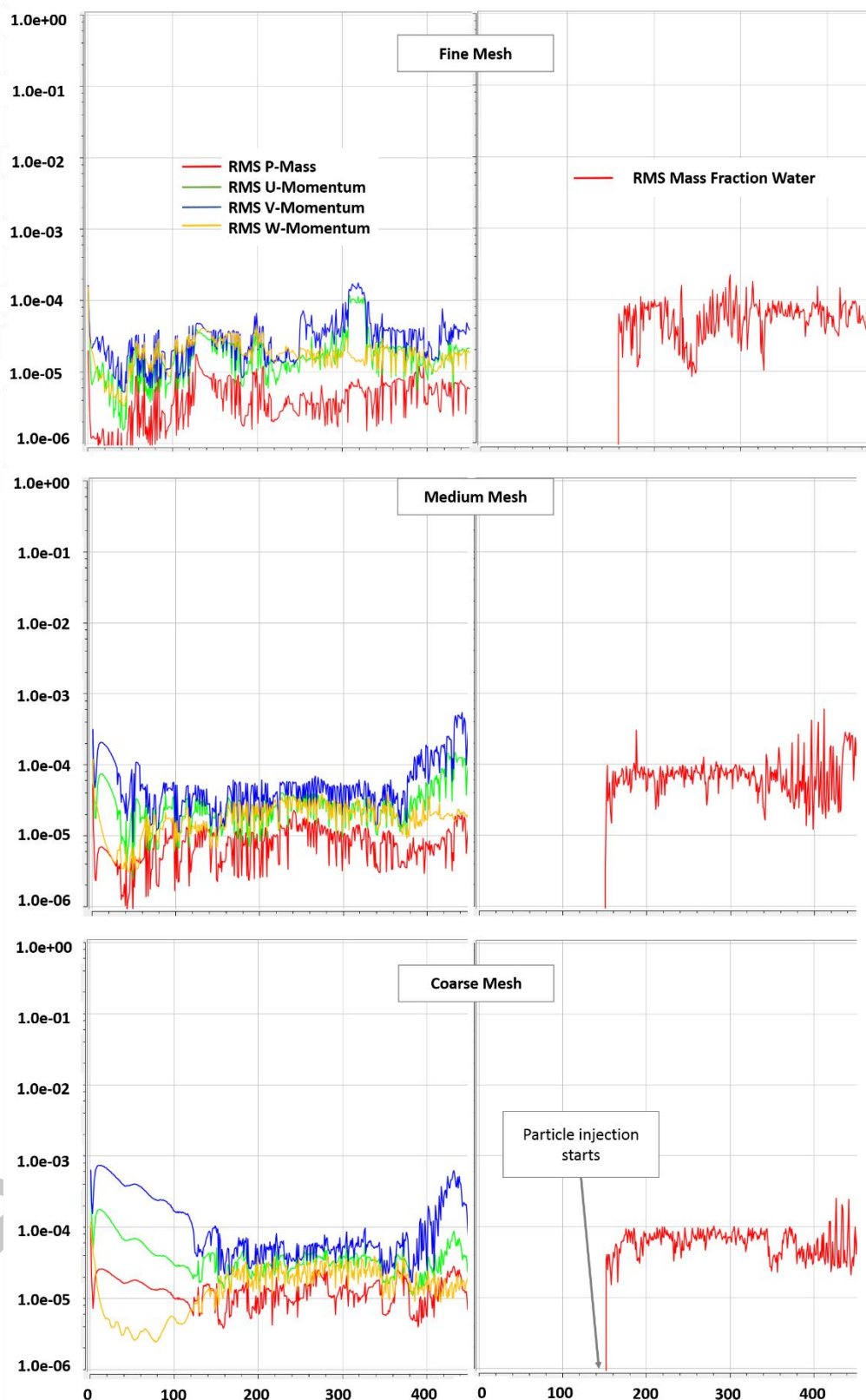
Figure 6 Up to 4.5 s were obtained using the simulation set-up described in section 3.3. The plot depicts the evolution of the residuals with the accumulated time step. All of the residuals were kept below the threshold level (10^{-3}) during the simulation.
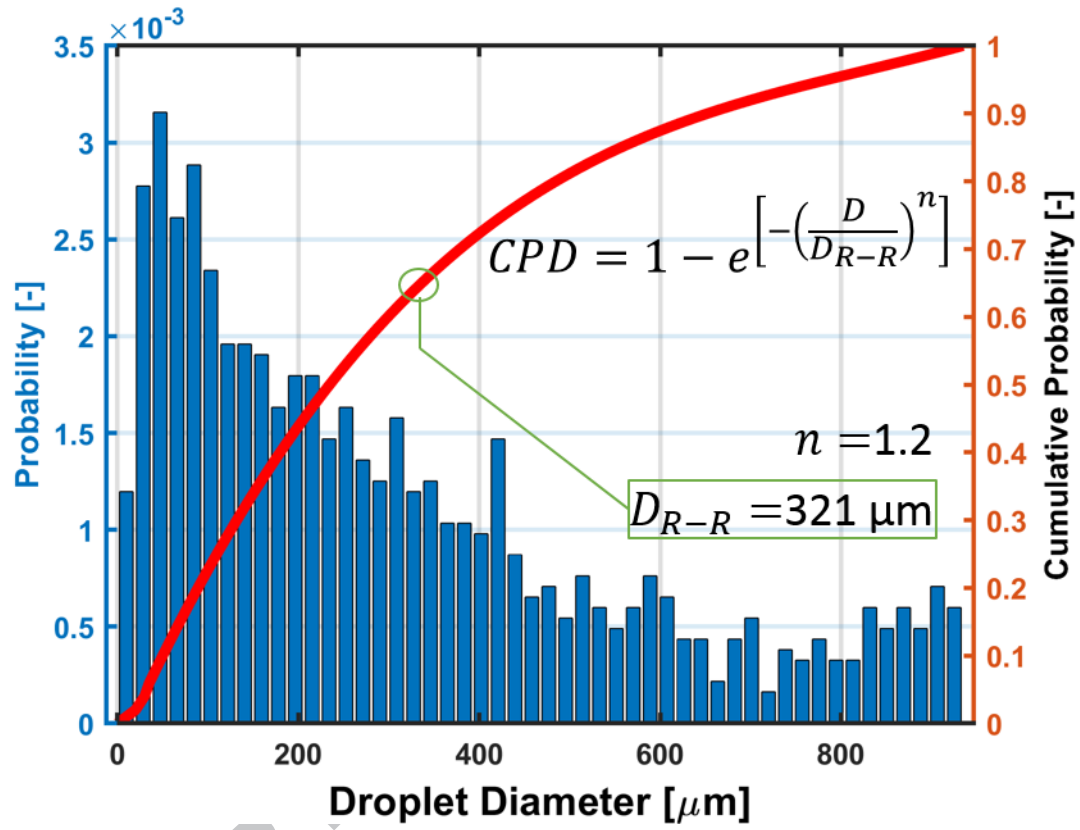
$$CPD = 1 - e^{\left[-\left(\frac{D}{D_{R-R}}\right)^n\right]}$$

$$n = 1.2$$

$$D_{R-R} = 321 \ \mu m$$

Figure 7 The cumulative droplet size distribution generated by the spray nozzle follows a Rosin-Rammler distribution with the parameters (D_{R-R} and n) indicated in the plot.
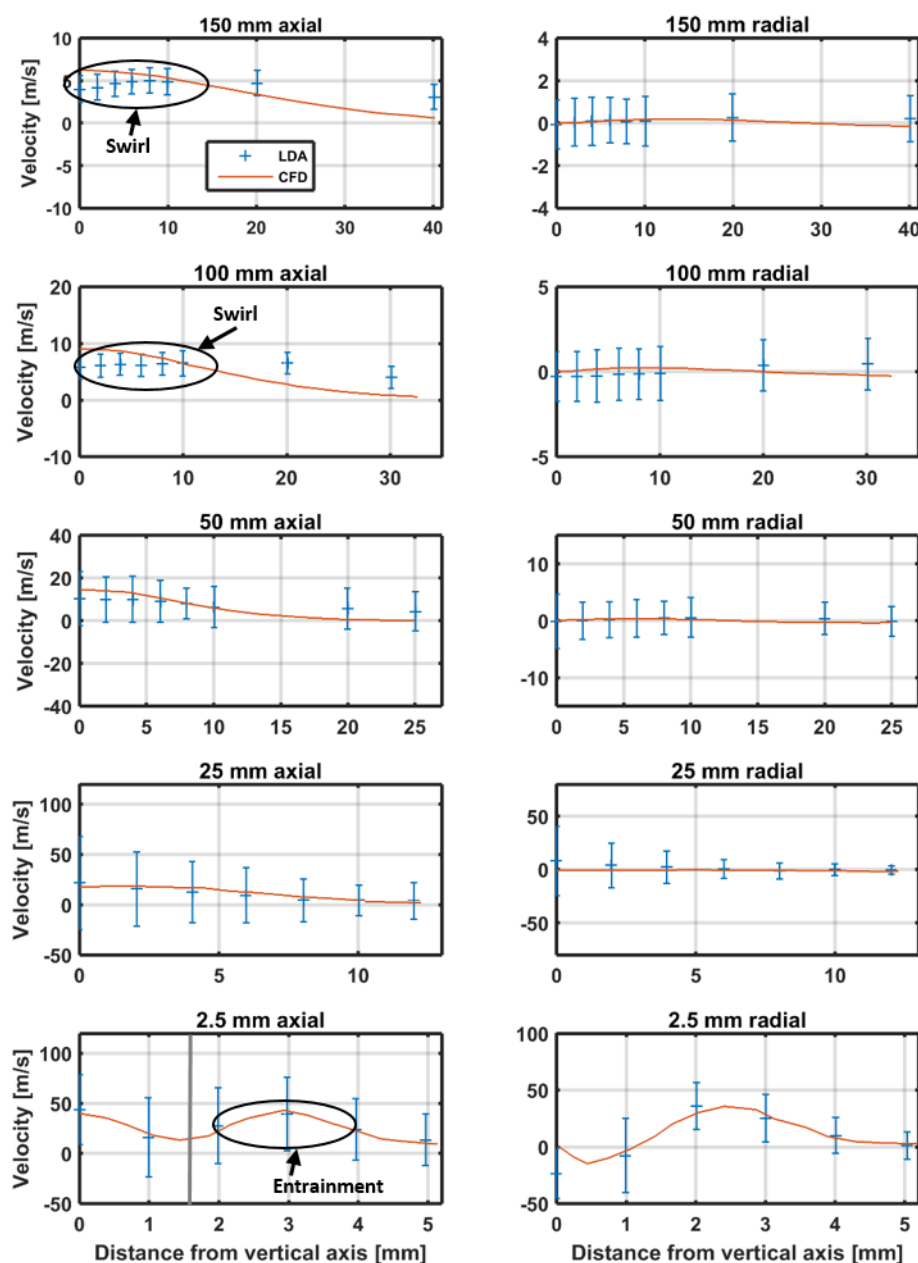
Figure 8 The experimental and numerical values obtained for the velocity field in the vicinity of the nozzle outlet at different vertical distances are compared in these plots. The column on the left-hand side represents the axial component of the gas velocity whereas the column on the right-hand side corresponds to the radial component. Each row corresponds to a different vertical distance on the vertical axis of the nozzle (2.5, 25, 50, 100, and 150 mm).
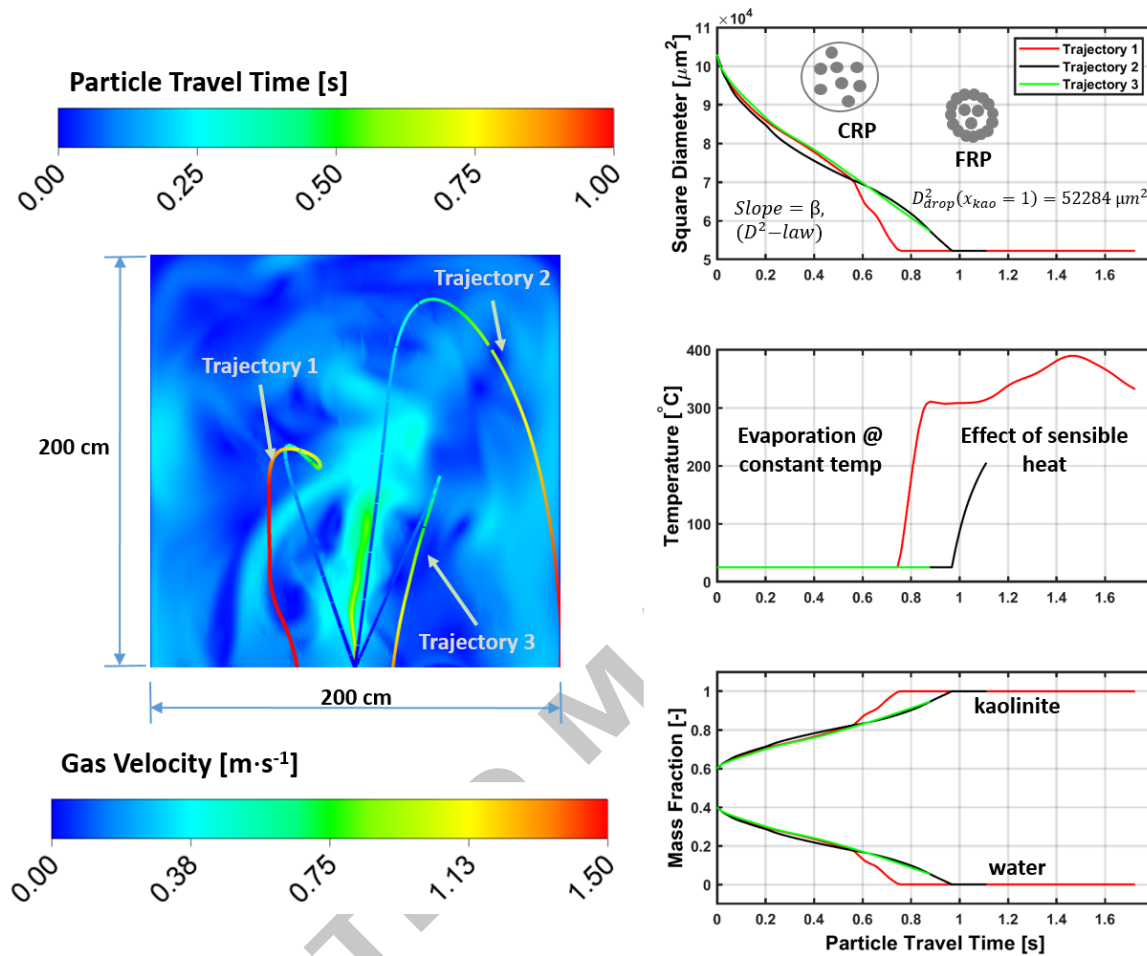
Figure 9 Plots of transient evolution of the square diameter, temperature, and concentration of both components (water and kaolinite), against particle travel time t_{travel} of the characteristic droplet (D_{R-R}=321 μm) at t_{flow}=4.27 s. The trajectories (color-coded with particle travel time) are depicted on a velocity map for the gas phase. Note that two separate legends, one for the velocity map of the gas phase and a different one for the particle travel time have been included.

LIST OF TABLES

Table 1 List of experiments and their defining parameters

Exp. #	Gauge Pressure [bar]	Vertical distance [mm]	Liquid flow rate [L·min^{-1}]
1	0.5	2	0.41
2	1.0	2	0.41
3	0.5	7.5	0.83
4	0.5	7.5	0.41
5	1.0	7.5	0.83
6	1.0	7.5	0.41
7	0.5	16	0.83
8	0.5	16	0.41
9	1.0	16	0.83
10	1.0	16	0.41

Table 2 Results and repeatability check of the Laser Diffraction droplet measurement. In order to facilitate a visual comparison the results, the effect of the air pressure and the vertical distance from the nozzle on the $\overline{SMD}$ of the slurry droplets is presented in subplot a), where the shaded areas gather those data points obtained with the same air pressure (0.41 L·min⁻¹): ▉ *marks 0.5 bar and* ▉ *marks 1 bar, both gauge pressure. In subplot b), an increase in the liquid flow rate results in a general increase of the droplet size distribution. The shaded areas gather data points at the same vertical distance from the nozzle and pressure:* ▉ *marks 16 mm & 0.5 bar,* ▉ *corresponds to 7.5 mm & 0.5 bar,* ▉ *16 mm & 1 bar, and* ▉ *7.5 mm and 1 bar.*

Exp. #	SMD [µm]			Range [µm]	$\overline{SMD}$ [µm]	ε_{rel}[%]
	Repetition 1	Repetition 2	Repetition 3			
1	71.82	71.73	71.84	0.11	71.80	0.15
2	56.35	56.35	56.33	0.02	56.34	0.04
3	55.34	55.50	56.17	1.20	55.89	1.49
4	41.68	41.80	42.21	0.53	41.93	1.27
5	43.11	43.23	44.10	0.99	43.49	2.28
6	34.09	33.86	33.66	0.43	33.90	1.27
7	56.31	56.47	56.30	0.28	56.42	0.30
8	47.39	47.74	47.46	0.35	47.51	0.74
9	46.32	46.27	46.44	0.17	46.34	0.37
10	39.65	39.32	39.35	0.33	39.41	0.84
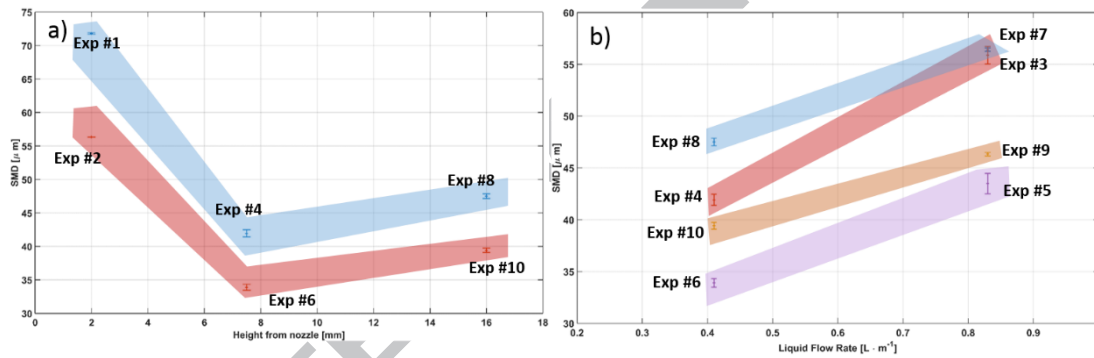
DECLARATION OF INTEREST STATEMENT

The authors declare that there is no conflict of interest regarding the publication of this article

HIGHLIGHTS

- Development of transient CFD model for production of barbotine ceramic powder
- Eulerian-Lagrangian model of droplet drying behaviour according to D^2-law
- Instant and location of crust formation within spray dryer captured numerically
- Numerical/experimental characterisation of velocity field generated by spray nozzle
- Rosin-Rammler size of droplets obtained experimentally and introduced into model